J|A|C|S ARTICLES

Published on Web 11/10/2009

Self-Assembly and Structure of Directly Imaged Inorganic-Anion Monolayers on a Gold Nanoparticle

Yifeng Wang,[†] Alevtina Neyman,[†] Elizabeth Arkhangelsky,[‡] Vitaly Gitis,[‡] Louisa Meshi,[§] and Ira A. Weinstock*,[†]

Department of Chemistry, Unit of Environmental Engineering, and Ilse Katz Institute for Nanoscale Science and Technology and Department of Materials Engineering, Ben Gurion University of the Negev, Beer Sheva, 84105, Israel

Received September 15, 2009; E-mail: iraw@bgu.ac.il

Abstract: Cryogenic "trapping" was used to obtain the first TEM images of self-assembled monolayers of inorganic anions on a gold nanoparticle. This unique structural information makes it possible to study the formation of a protecting-ligand shell at an unprecedented level of detail. The protecting ligands are polyoxometalates (POMs; α-$X^{n+}W_{12}O_{40}^{(8-n)-}$, $X^{n+} = Al^{3+}$ and "$2H^{+}$", and α-$X^{n+}W_{11}O_{39}^{(12-n)-}$, $X^{n+} = P^{5+}$, Si^{4+}, and Al^{3+}) with large negative charges for association with the gold surface and W atoms ($Z = 74$) for TEM imaging. The POM-anion shells were obtained by ligand exchange from citrate-protected 13.8 nm gold nanoparticles. Replacement of the organic (citrate) by inorganic (tungsten-oxide) ligand shells results in substantial changes in the surface plasmon resonance (SPR). By correlating cryo-TEM images with changes in the SPR, degrees of surface coverage were reliably quantified by UV−visible spectroscopy. Then, the kinetics and thermodynamics of ligand-shell formation were investigated by systematically varying POM structure and charge. Rates of POM association with the gold surface ("nucleation") are inhibited by the electric-potential barrier of the citrate-stabilized particles, while binding affinities increase *linearly* with the charges (from 5- to 9-) of structurally different POM anions, suggesting that no single orientation ("lattice matching") is required for monolayer self-assembly. Time-dependent cryo-TEM images reveal that monolayer growth occurs via "islands", a mechanism that points to cation-mediated attraction between bound POMs. Complete ligand shells comprised of 330 molecules of α-$AlW_{11}O_{39}^{9-}$ (**1**) possess small net charges (29*e* from zeta-potential measurements) and short Debye lengths ($\kappa^{-1} = 1.0$ nm), which indicate that ~99% of the 2970 K^+ counter cations lie within ca. 1.5 nm (~3 hydrated K^+ ion diameters) from the outer surface of the POM shell. Energetic analysis of the 1.57 ± 0.04 nm center-to-center distance between molecules of **1** further indicates that K^+ ions reside in the ca. 4.5 Å spaces between the bound ligands. These findings reveal an important structural role for counter cations within POM ligand shells on gold nanoparticles, analogous to that for cations in the monolayer walls of *hollow* POM-macroanion vesicles.

Introduction

While organic[1] and inorganic[2] monolayers have been characterized at the subnanometer scale on planar surfaces, the acquisition of similarly detailed information about organizations of protecting ligands on curved nanoparticle surfaces remains a challenge. Spectroscopic and chemical methods have provided important information about alkanethiol ligand shells.[1b,3] Meanwhile, *direct images*[4] of organic ligands on gold nanoparticles are extremely difficult to obtain. Even less is known[1b] about the formation and structural organizations of protective monolayers comprised of inorganic ligands. To address this, we recently[5] deployed small (1.12-nm diameter) tungsten-oxide

[†] Department of Chemistry.
[‡] Unit of Environmental Engineering.
[§] Ilse Katz Institute for Nanoscale Science and Technology and Department of Materials Engineering.

(1) (a) Tao, F.; Bernasek, S. L. *Chem. Rev.* **2007**, *107*, 1408–1453. (b) Love, J. C.; Estroff, L. A.; Kriebel, J. K.; Nuzzo, R. G.; Whitesides, G. M. *Chem. Rev.* **2005**, *105*, 1103–1170. (c) Poirier, G. E. *Chem. Rev.* **1997**, *97*, 1117–1128.

(2) (a) Fleming, C.; Long, D.; McMillan, N.; Johnston, J.; Bovet, N.; Dhanak, V.; Gadegaard, N.; Kögerler, P.; Cronin, L.; Kadodwala, M. *Nat. Nanotech.* **2008**, *3*, 229–233. (b) Kim, J.; Gewirth, A. A. *Langmuir* **2003**, *19*, 8934–8942. (c) Lee, L.; Wang, J. X.; Adzic, R. R.; Robinson, I. K.; Gewirth, A. A. *J. Am. Chem. Soc.* **2001**, *123*, 8838–8843. (d) Tang, Z.; Liu, S.; Wang, E.; Dong, S. *Langmuir* **2000**, *16*, 4946–4952. (e) Klemperer, W. G.; Wall, C. G. *Chem. Rev.* **1998**, *98*, 297–306. (f) Kaba, M. S.; Song, I. K.; Duncan, D. C.; Hill, C. L.; Barteau, M. A. *Inorg. Chem.* **1998**, *37*, 398–406. (g) Ge, M.; Zhong, B.; Klemperer, W. G.; Gewirth, A. A. *J. Am. Chem. Soc.* **1996**, *118*, 5812–5813. (h) Rong, C.; Anson, F. C. *Anal. Chem.* **1994**, *66*, 3124–3130. (i) Keita, B.; Nadjo, L. *J. Electroanal. Chem.* **1993**, *354*, 295–304.

(3) (a) Murray, R. W. *Chem. Rev.* **2008**, *108*, 2688–2720. (b) Laaksonen, T.; Ruiz, V.; Liljeroth, P.; Quinn, B. M. *Chem. Soc. Rev.* **2008**, *37*, 1836–1846. (c) Dahl, J. A.; Maddux, B. L. S.; Hutchison, J. E. *Chem. Rev.* **2007**, *107*, 2228–2269. (d) Laaksonen, T.; Pelliniemi, O.; Quinn, B. M. *J. Am. Chem. Soc.* **2006**, *128*, 14341–14346. (e) Daniel, M. C.; Astruc, D. *Chem. Rev.* **2004**, *104*, 293–346.

(4) (a) Carney, R. P.; DeVries, G. A.; Dubois, C.; Kim, H.; Kim, J. Y.; Singh, C.; Ghorai, P. K.; Tracy, J. B.; Stiles, R. L.; Murray, R. W.; Glotzer, S. C.; Stellacci, F. *J. Am. Chem. Soc.* **2008**, *130*, 798–799. (b) Heaven, M. W.; Dass, A.; White, P. S.; Holt, K. M.; Murray, R. W. *J. Am. Chem. Soc.* **2008**, *130*, 3754–3755. (c) Jadzinsky, P. D.; Calero, G.; Ackerson, C. J.; Bushnell, D. A.; Kornberg, R. D. *Science* **2007**, *318*, 430–433. (d) Jackson, A. M.; Hu, Y.; Silva, P. J.; Stellacci, F. *J. Am. Chem. Soc.* **2006**, *128*, 11135–11149. (e) Jackson, A. M.; Myerson, J. W.; Stellacci, F. *Nat. Mater.* **2004**, *3*, 330–336.

10.1021/ja907815d CCC: $40.75 © **2009 American Chemical Society**

clusters as protecting anions and used cryogenic "trapping" and transmission-electron microscopy (cryo-TEM) to obtain the first images of inorganic-ligand monolayers on silver particles in their native solution state.

The tungsten-oxide protecting anions are polyoxometalates[6] (POMs) that possess large negative charges for association with metal(0) surfaces and W atoms ($Z = 74$) for effective TEM imaging. Early reports document the use of POMs to stabilize both colloidal silver halides[7] and Ag(0) nanoparticles,[8] and pioneering work involving POMs as protecting ligands for Ir(0) and Rh(0) nanoparticles, and applications of these in catalysis, was carried out by Finke.[9] This was followed by important advances in synthesis and catalysis by many groups, who extended this growing class of functional materials to include a wide range of POMs and late-transition metal(0) nanoparticles.[10] While the basis for their unique catalytic properties is not yet clear, it likely derives from the redox properties of the POM complexes,[2a,11] in combination with the ability of these metal-oxide clusters—like oxide supports in heterogeneous catalysis[9d]—to modify the activities of atoms on the surfaces of metal(0) particles.[12]

We now use POM cluster anions, in combination with cryo-TEM imaging[13] and spectroscopic and other solution-state methods,[14] to provide the first detailed account of the kinetics, thermodynamics, growth and surface organization of a structurally characterized protecting-ligand shell on a gold nanoparticle. This is achieved using a series of POMs[14a] whose structures and charges can be systematically varied. Namely, main-group heteroatoms, X^{n+} (= Al^{3+} and "$2H^{+}$"), at the center of the plenary alpha-Keggin structure, α-$X^{n+}W_{12}O_{40}^{(8-n)-}$, provide anions with charges of 5- and 6-, respectively, while for the monodefect derivative of the alpha-Keggin structure, α-$X^{n+}W_{11}O_{39}^{(12-n)-}$, the heteroatoms, $X^{n+} = P^{5+}$, Si^{4+} and Al^{3+}, provide respective charges of 7-, 8- and 9- (Figure 1).

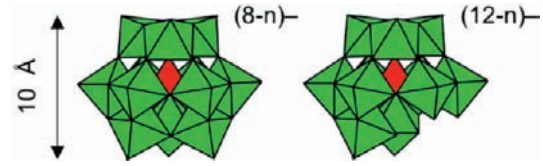

Figure 1. Structures of plenary and monodefect derivatives of alpha-Keggin anions, with overall charges indicated as functions of the positive charge of the central heteroatom, X^{n+}. The structures are in polyhedral notation: W(VI) atoms are at the centers of the green polyhedra, and the main-group heteroatoms reside in a tetrahedral site (red) at the center of each structure. Oxygen atoms lie at the vertices of the polyhedra. (Left) α-$X^{n+}W_{12}O_{40}^{(8-n)-}$, X^{n+} = Al^{3+} and "$2H^{+}$", which have charges of 5- and 6-; (Right) α-$X^{n+}W_{11}O_{39}^{(12-n)-}$, $X^{n+} = P^{5+}$, Si^{4+}, Al^{3+}, with charges of 7-, 8- and 9-. The "defect" at the lower right of this structure (a single "$W=O^{4+}$" moiety is "absent") leaves 4 (formally) terminal $W-O^{-}$ ligands that can participate in binding to metal(0) surfaces.

The POM-monolayers are prepared from citrate-protected 13.8-nm diameter gold nanoparticles by ligand exchange[10g,h,15] in water. Due to differences in their refractive indices, replacement of the organic (citrate) by inorganic (tungsten-oxide) ligand shells results in a substantial change in the absorbance maximum of the surface plasmon resonance (SPR).[16] Hence, by combining UV−visible spectroscopy of the SPR with direct (cryo-TEM) imaging of surface coverage (Θ), changes in SPR predicted by Mie theory can be quantitatively correlated with ligand-shell composition and structure.

This and additional solution-state methods make it possible to investigate the following fundamental phenomena: (1) the effect of anion charge on rates of initial association with the gold surface (nucleation), (2) the relative importance of ligand structure versus charge on binding to gold atoms on the nanoparticle surface, (3) monolayer growth ("island"[17] versus "filling-in" mechanisms), (4) monolayer stability, and (5) the role of counter cations and electrostatic interactions within the inorganic-polyelectrolyte ligand shell. The results reveal an important *structural* role for counterions in the self-assembly of charged molecules on metal-nanoparticle surfaces.

Materials and Methods

Materials. The polyoxometalate (POM) salts, α-$K_9Al^{III}W_{11}O_{39}\cdot 13H_2O$ (K_9**1**),[18] α-$K_8Si^{IV}W_{11}O_{39}\cdot 13H_2O$ (K_8**2**),[19] α-$K_7P^{V}W_{11}O_{39}\cdot 12H_2O$ (K_7**3**)[20] and α-$Na_5Al^{III}W_{12}O_{40}\cdot 17H_2O$ (Na_5**5**)[18] were prepared using published methods and recrystallized three times from water before use. Sodium polytungstate hydrate, $Na_6H_2W_{12}O_{40}\cdot$

(5) Neyman, A.; Meshi, L.; Zeiri, L.; Weinstock, I. A. *J. Am. Chem. Soc.* **2008**, *130*, 16480–16481.
(6) (a) Pope, M. T. In *Comp. Coord. Chem. II: From Biology to Nanotechnology*; Wedd, A. G., Ed.; Elsevier: Oxford, 2004; Vol. 4; pp 635−678. (b) Hill, C. L. In *Comp. Coord. Chem. II: From Biology to Nanotechnology*; Wedd, A. G., Ed.; Elsevier: Oxford, 2004; Vol. 4; pp 679−759.
(7) Matijevic, E.; Mathai, K. G.; Kerker, M. *J. Phys. Chem.* **1963**, *67*, 1995–1999.
(8) Siiman, O.; Feilchenfeld, H. *J. Phys. Chem.* **1988**, *92*, 453–464.
(9) (a) Graham, C. R.; Ott, L. S.; Finke, R. G. *Langmuir* **2009**, *25*, 1327–1336. (b) Finke, R. G.; Özkar, S. *Coord. Chem. Rev.* **2004**, *248*, 135–146. (c) Aiken, J. D.; Finke, R. G. *J. Am. Chem. Soc.* **1999**, *121*, 8803–8810. (d) Lin, Y.; Finke, R. G. *J. Am. Chem. Soc.* **1994**, *116*, 8335–8353.
(10) (a) Dolbecq, A.; Compain, J. D.; Mialane, P.; Marrot, J.; Sécheresse, F.; Keita, B.; Holzle, L. R. B.; Miserque, F.; Nadjo, L. *Chem.−Eur. J.* **2009**, *15*, 733–741. (b) Troupis, A.; Triantis, T.; Hiskia, A.; Papaconstantinou, E. *Eur. J. Inorg. Chem.* **2008**, 5579–5586. (c) Maayan, G.; Neumann, R. *Catal. Lett.* **2008**, *123*, 41–45. (d) Costa-Coquelard, C.; Schaming, D.; Lampre, I.; Ruhlmann, L. *Appl. Catal. B: Environ.* **2008**, *84*, 835–842. (e) Boujday, S.; Blanchard, J.; Villanneau, R.; Krafft, J.; Geantet, C.; Louis, C.; Breysse, M.; Proust, A. *ChemPhysChem* **2007**, *8*, 2636–2642. (f) Keita, B.; Zhang, G.; Dolbecq, A.; Mialane, P.; Sécheresse, F.; Miserque, F.; Nadjo, L. *J. Phys. Chem. C* **2007**, *111*, 8145–8148. (g) Ernst, A. Z.; Sun, L.; Wiaderek, K.; Kolary, A.; Zoladek, S.; Kulesza, P. J.; Cox, J. A. *Electroanalysis* **2007**, *19*, 2103–2109. (h) Lica, G. C.; Browne, K. P.; Tong, Y. *J. Cluster Sci.* **2006**, *17*, 349–359. (i) Maayan, G.; Neumann, R. *Chem. Commun.* **2005**, 4595–4597. (j) Mandal, S.; Selvakannan, P. R.; Pasricha, R.; Sastry, M. *J. Am. Chem. Soc.* **2003**, *125*, 8440–8441. (k) Troupis, A.; Hiskia, A.; Papaconstantinou, E. *Angew. Chem., Int. Ed.* **2002**, *41*, 1911–1914.
(11) (a) Geletii, Y. V.; Hill, C. L.; Bailey, A. J.; Hardcastle, K. I.; Atalla, R. H.; Weinstock, I. A. *Inorg. Chem.* **2005**, *44*, 8955–8966. (b) Weinstock, I. A. *Chem. Rev.* **1998**, *98*, 113–170.
(12) Min, B. K.; Friend, C. M. *Chem. Rev.* **2007**, *107*, 2709–2724.
(13) (a) Pouget, E. M.; Bomans, P. H. H.; Goos, J. A. C. M.; Frederik, P. M.; de With, G.; Sommerdijk, N. A. J. M. *Science* **2009**, *323*, 1455–1458. (b) Omer, L.; Ruthstein, S.; Goldfarb, D.; Talmon, Y. *J. Am. Chem. Soc.* **2009**, *131*, 12466–12473. (c) Baytekin, H. T.; Baytekin, B.; Schulz, A.; Springer, A.; Gross, T.; Unger, W.; Artamonova, M.; Schlecht, S.; Lentz, D.; Schalley, C. A. *Chem. Mater.* **2009**, *21*, 2980–2992. (d) Kumar, S.; Wang, Z.; Penn, R. L.; Tsapatsis, M. *J. Am. Chem. Soc.* **2008**, *130*, 17284–17286. (e) Nativ-Roth, E.; Yerushalmi-Rozen, R.; Regev, O. *Small* **2008**, *4*, 1459–1467.
(14) (a) Geletii, Y. V.; Hill, C. L.; Atalla, R. H.; Weinstock, I. A. *J. Am. Chem. Soc.* **2006**, *128*, 17033–17042. (b) Grigoriev, V. A.; Cheng, D.; Hill, C. L.; Weinstock, I. A. *J. Am. Chem. Soc.* **2001**, *123*, 5292–5307.
(15) (a) Ji, X.; Copenhaver, D.; Sichmeller, C.; Peng, X. *J. Am. Chem. Soc.* **2008**, *130*, 5726–5735. (b) Woehrle, G. H.; Brown, L. O.; Hutchison, J. E. *J. Am. Chem. Soc.* **2005**, *127*, 2172–2183. (c) Song, Y.; Murray, R. W. *J. Am. Chem. Soc.* **2002**, *124*, 7096–7102.
(16) (a) Ha, J.; Katz, A.; Drapailo, A. B.; Kalchenko, V. I. *J. Phys. Chem. C* **2009**, *113*, 1137–1142. (b) Ha, J.; Solovyov, A.; Katz, A. *Langmuir* **2009**, *25*, 153–158. (c) Homola, J. *Chem. Rev.* **2008**, *108*, 462–493. (d) Ghosh, S. K.; Pal, T. *Chem. Rev.* **2007**, *107*, 4797–4862. (e) Miller, M. M.; Lazarides, A. A. *J. Phys. Chem. B* **2005**, *109*, 21556–21565.
(17) Poirier, G. E.; Pylant, E. D. *Science* **1996**, *272*, 1145–1148.

xH_2O (Na_6**4**), $HAuCl_4$ (99.9+%) and trisodium citrate, $C_6H_5Na_3O_7 \cdot 2H_2O$ (analytical grade; Na_3Ct) were obtained from Sigma-Aldrich. All other materials used for synthesis were obtained from commercial sources and used as received. The purities of the POM salts were checked (as appropriate) by IR, Raman, ^1H, ^{27}Al, and ^{31}P NMR spectroscopy, and by cyclic voltammetry. All glassware used for synthesis and storage of gold nanoparticles was pretreated with fresh aqua regia (1:3 v/v ratio of HCl to HNO_3). All solutions were prepared using 18 MΩ water (Millipore Direct-Q), and added salts or buffers were of the highest purity available.

Instrumentation. UV−vis spectra were obtained using a Hewlett-Packard 8452A spectrophotometer equipped with a diode-array detector. NMR spectra were acquired in D_2O/water mixtures using a Brüker 500 MHz instrument. Fourier-transform infrared (FTIR) spectra were obtained on a Nicolet Impact 410 spectrophotometer (KBr pellets), and Raman spectra were obtained on a Jobin-Yvon LabRam HR 800 micro-Raman system. Zeta potential measurements were obtained using a ZetaPlus instrument from the Brookhaven Instrument Co. TEM measurements were performed on a FEI Tecnai 12 G^2 electron microscope, working under an acceleration voltage of 120 kV.

Cryogenic Sample Preparation for Transmission Electron Spectroscopy (Cryo-TEM). Cryogenically frozen samples were prepared using a fully automated vitrification device (Vitrobot, FEI). First, 5 μL of the sample solution was placed by pipet onto a glow discharged Cu grid covered with a lacey-carbon film, held inside a 100%-humidity chamber. The grid was mechanically "blotted" and immediately plunged into liquid ethane (mp 90.34 K) cooled by liquid nitrogen (77.2 K). Cryo-TEM images were captured on the FEI Tecnai 12 G^2 instrument (120 kV) using a Gatan slow-scan camera. Image brightness and contrast were adjusted using DigitalMicrograph.

Preparation of Citrate-Protected Gold Nanoparticles (Au NPs). The Turkevich method[21] was used after minor modification. After heating 100 mL of 5×10^{-4} M $HAuCl_4$ to boiling on a hot plate, 0.2 mL of 1 M trisodium citrate was added quickly with vigorous stirring. The faint yellowish color of $HAuCl_4$ disappeared immediately and changed to wine-red after about 5 min. The solution was heated with stirring for another 25 min to ensure complete conversion of $HAuCl_4$ to Au(0), removed from the hot plate, and allowed to cool to room temperature. After the addition of water (as needed) to restore the volume to 100 mL, the solution was stored in the dark at room temperature. The Au NPs had an average diameter of 13.8 ± 0.9 nm, based on TEM measurements (Figure S1, Supporting Information), and no observable difference in size, size distribution, or reactivity were observed in different batches of the Au NPs. When different batches were used, however, their concentrations were calibrated spectrophotometrically. For this purpose, a calibration curve was made from a quantitatively prepared and diluted Au NP solution. Before use, all newly prepared Au NP solutions were diluted as indicated by this calibration curve.

Preparation of α-$K_9AlW_{11}O_{39}$ ($K_9$1) Monolayer-Protected Au NPs. A volume of 1.5 mL of K_9**1** (4 mM in water; natural pH = 7.3 ± 0.1) was added with stirring to a vial containing 1.5 mL of a pH 6.1 ± 0.1 solution of citrate-protected Au NPs (0.5 mM Au, 6.2×10^{-9} M Au NPs based on an average diameter of 13.8 nm). After completion of reaction (20 h), pH values were 7.2 ± 0.2, and the solutions were stored in the dark at room temperature. Notably, **1** is stable to acid condensation or base hydrolysis at pH values of from 5 to 9. Nevertheless, the structural integrity of **1** after reaction with the Au NPs was confirmed by ^{27}Al NMR: no signals associated with condensation or hydrolysis of **1** to $AlW_{12}O_{40}^{5-}$ or $Al(Al)W_{11}O_{39}^{6-}$, respectively, were observed.[18] During reaction with **1**, zeta potential values changed from −31.5 ± 4.5 mV for the citrate-protected particles (pH = 6.0), to −62.1 ± 7.5 mV (pH 7.2), and monolayer formation by **1** was confirmed by cryo-TEM (see images in text).

Zeta Potential Measurements. Zeta potentials were measured at least 24 h after mixing POM salts with the Au NPs. To obtain accurate zeta potential values, the manufacturer-supplied BI-ZR3 solution was used as a reference, after which, 20 repeat measurements were obtained using the POM-protected Au NP solutions. After discarding any obviously incorrect values, the mean value of accepted measurements and its statistical uncertainty, was taken as the zeta potential.

Surface-Coverage Calculations. To our knowledge, changes in the SPR absorbance—while used extensively[16c,22] to quantify adsorbate coverage on planar surfaces, and for numerous metal-nanoparticle[16a,b] systems and sensor applications—have not been used to quantify *surface coverage* of metal nanoparticles. Mie theory[16c−e,23] describes the absorption of light by nanoparticles that are small relative to the wavelength of visible light (diameters between 3 and tens of nanometers). In this size range the quasi-static approximation is applicable, i.e., the scattering of visible light is not significant, and the electric field of the incident light is considered uniform and static. A homogeneous and isotropic sphere placed in the uniform and static field $\mathbf{E_0}$ is polarized and has a dipole moment **p** proportional to the applied field (eq 1).

$$\mathbf{p} = \varepsilon_m \alpha \mathbf{E}_0 \tag{1}$$

In eq 1, α is defined as the polarizability, $4\pi r_s^3(\varepsilon_s - \varepsilon_m)/(\varepsilon_s + 2\varepsilon_m)$; r_s is the radius of the sphere; ε_s and ε_m are the permittivity of the sphere and the surrounding medium, respectively. From eq 1, geometrical analysis based on cryo-TEM images of structurally characterized POM-protected Au NPs was used to obtain an expression for the effect of surface coverage on the intensity of the surface plasmon resonance (see Supporting Information for the full derivation). The result is that at a given surface coverage Θ, the absorbance, A, at a wavelength λ (where $\lambda \gg$ particle size) can be expressed as shown in eq 2.

$$A = (1 - \Theta)A_0 + \Theta A_1 \tag{2}$$

Here, $A = A_0$ for $\Theta = 0$, and $A = A_1$ for $\Theta = 1$ ($\Theta = 1$ refers to full monolayer coverage). According to eq 2, the absorbance, A, increases linearly with the degree of surface coverage by the POM ligands. Rearrangement of eq 2 gives eq 3, which is a structurally based relationship between changes in the surface plasmon resonance (SPR) and degrees of surface coverage.

$$\Theta = (A - A_0)/(A_1 - A_0) \tag{3}$$

Confirmation of this model by cryo-TEM images of partially covered gold nanoparticles is provided in the Results section.

(18) (a) Cowan, J. J.; Hill, C. L.; Reiner, R. S.; Weinstock, I. A. *Inorg. Synth.* **2002**, *33*, 18–26. (b) Cowan, J. J.; Bailey, A. J.; Heintz, R. A.; Do, B. T.; Hardeastle, K. I.; Hill, C. L.; Weinstock, I. A. *Inorg. Chem.* **2001**, *40*, 6666–6675. (c) Weinstock, I. A.; Cowan, J. J.; Barbuzzi, E. M. G.; Zeng, H. D.; Hill, C. L. *J. Am. Chem. Soc.* **1999**, *121*, 4608–4617.

(19) Tézé, A.; Hervé, G.; Finke, R. G.; Lyon, D. K. *Inorg. Synth.* **1990**, *27*, 85–96.

(20) Haraguchi, N.; Okaue, Y.; Isobe, T.; Matsuda, Y. *Inorg. Chem.* **1994**, *33*, 1015–1020.

(21) Kimling, J.; Maier, M.; Okenve, B.; Kotaidis, V.; Ballot, H.; Plech, A. *J. Phys. Chem. B* **2006**, *110*, 15700–15707.

(22) (a) Scodeller, P.; Flexer, V.; Szamocki, R.; Calvo, E. J.; Tognalli, N.; Troiani, H.; Fainstein, A. *J. Am. Chem. Soc.* **2008**, *130*, 12690–12697. (b) Sassolas, A.; Leca-Bouvier, B. D.; Blum, L. J. *Chem. Rev.* **2008**, *108*, 109–139. (c) Kalyuzhny, G.; Schneeweiss, M. A.; Shanzer, A.; Vaskevich, A.; Rubinstein, I. *J. Am. Chem. Soc.* **2001**, *123*, 3177–3178. (d) Eck, D.; Helm, C. A.; Wagner, N. J.; Vaynberg, K. A. *Langmuir* **2001**, *17*, 957–960. (e) Raether, H. *Surface Plasmons on Smooth and Rough Surfaces and on Gratings*; Springer Verlag: Berlin, 1988.

(23) Bohren, C. F.; Huffman, D. R. *Absorption and Scattering of Light by Small Particles*; John Wiley & Sons: New York, 1983.

Langmuir Isotherms for Monolayer Formation. Langmuir isotherms are routinely used to quantify degrees of surface coverage (Θ) as functions of adsorbate concentration in solution or the gas phase. Surface-coverage values, Θ, (from UV−vis spectroscopic analysis of changes in the SPR; eq 3) are correlated with solution concentrations of adsorbates using eq 4, where C is the bulk-solution concentration of the species being adsorbed (i.e., the POM anion) and K is a constant.

$$\Theta = KC/(1 + KC) \tag{4}$$

Combining eqs 3 and 4 gives eq 5, where C and K have the same meanings as in eq 4, and A_0 and A_1 correspond to no associated POM ligands, and to complete POM-monolayer coverage, respectively.

$$A = (A_0 + KA_1C)/(1 + KC) \tag{5}$$

Experimentally, maximum variations in A (i.e., $\Delta A_{max} = A_1 - A_0$) increase with POM charge. This could be due to differences in the refractive indices of the POM anions themselves, or to effects of POM charge on the structure and composition of the Stern layer and of the diffuse layer of counter-cations more loosely associated with the POM shell. Data for use in eq 5 were obtained by adding aliquots of POM-salt solutions to citrate-protected 13.8-nm Au NPs. For this, POM and Au NPs solutions (1.5 mL of each) were quickly added to a vial and mixed by shaking for several seconds. A series of vials containing incrementally larger POM concentrations were prepared and stored in the dark at room temperature (23 ± 1 °C). UV−visible spectra were obtained after one day. Concentrations of POMs in the bulk solutions, [POM], were at least an order of magnitude larger than the number of available binding sites on the Au NPs ([site], which for routinely used Au NP solutions was 1.0×10^{-6} M based on Au concentration, particle size and cryo-TEM images; see Results section). Therefore, concentrations of *adsorbed* POM anions were neglected when using eq 5 to evaluate absorbance versus [POM] data.

Kinetic Studies. Kinetic data were obtained using an SX20 Stopped-Flow Spectrometer (Applied Photophysics Ltd., UK) equipped with a photomultiplier and a photodiode array detector. A JULABO F12-ED circulating-bath temperature controller was used to maintain specified temperatures to within ± 0.1 °C. Cell path lengths were 10 mm. The volume ratio of the POM and Au NPs solutions was always 1:1. To measure initial rates, single-wavelength traces were recorded with the photomultiplier set at 520 nm. Each experimental run was repeated more than 20 times and some obviously bad traces were discarded. Due to short, irreproducible absorbance changes at the start of each trace, the first few seconds were ignored (usually 4 s for K_9**1**, and less than 1 s for K_8**2** and K_7**3**). Provided that sufficiently small POM concentrations were used, these plots were effectively linear over the subsequent 10 s of reaction. Initial rates, r_i, and their standard deviations were calculated by linear fitting of the absorbance versus time plots. Changes in SPR absorbance were converted to molar concentrations of gold-surface-bound POM anions to give initial-rate values defined as shown in eq 6. The total concentration of POM binding sites, [site], in solutions of the 13.8 nm Au NPs was determined as noted above. Therefore, concentrations of *adsorbed* POM anions after 10 s were readily determined from percentage-changes in the SPR.

$$r_i = \text{molar concentration of adsorbed POM molecules}/\Delta t \tag{6}$$

The pH values of the citrate-protected Au NP solution were between 6.0 and 6.2, and the natural pH values of the three POM solutions used in initial-rate studies were 7.3, 6.4, and 6.0, for K_9**1**, K_8**2**, and K_7**3**, respectively. Control experiments (see Figure S2, Supporting Information) showed that the SPR absorption was not influenced by pH (between values of 6 and 7.5), after which the POM solutions were used at their natural pH values.

Preliminary kinetic data showed that rates increased nonlinearly with ionic strength (see Figure S3, Supporting Information). Therefore, to obtain reliable results, a citrate buffer ($H_3Ct + Na_3Ct$) was used to maintain ionic strength. Citrate was used because it did not cause aggregation of the Au NPs, and Figure S4 (Supporting Information) shows that variation of [citrate] over the range used did not result in kinetic inhibition. For determining the dependence of reaction rates on concentrations of Au NPs, a constant concentration of 0.3 mM **1** was used, and the [Au NP] ranged from 1.0 to 5.2×10^{-9} M. Citrate buffer was added to the Au NP solutions prior to mixing with **1**, so that all reactions were carried out at an ionic strength of 15.3 mM. For determining rates as a function of [POM], concentrations of Au NPs were constant (3.1×10^{-9} M), and [POM] values ranged from 0.05 to 0.30 mM. Final ionic strength values after mixing the Au NPs and POM solutions (constant for each POM used) were 17.6 for reactions of **1**, 14.9 mM for **2** and 12.2 mM for **3**. This small decrease in ionic strength values (between sets of kinetic experiments) reflects the decreases in charges of the three POM anions, from 9- to 8- to 7-.

For long-term kinetics (monolayer formation), multiple wavelength traces were recorded using the stopped-flow instrument's photodiode array detector. For long reactions (up to several hours), absolute absorbance values provided by the instrument's diode-array detector were less accurate (stable with time) than those obtained using the HP 8452A spectrophotometer. Therefore, final absorbance-plateau values from the stopped-flow were calibrated based on data from the HP instrument, and final traces were adjusted accordingly.

Time-Dependent Cryo-TEM Study of Monolayer Growth. Prior to cryo-TEM imaging, the progress of self-assembly was tracked spectroscopically to determine the time needed after addition of **1** (0.13 mM) to reach 40% POM coverage ($\Theta = 0.4$). Using these parameters, solutions of K_9**1** and of the citrate-protected Au NPs (0.25 mM Au) were combined at $t = 0$, and at the determined time (5000 s after mixing), the evolving solution-state structure was cryogenically cooled.

Results

In section 1 (below), cryogenic sample preparation for transmission electron microscopy (cryo-TEM) is used to obtain images of inorganic-anion monolayers on a gold nanoparticle. Statistical analysis of *directly imaged* organizations of individual POM ligands is then used to provide a structurally based correlation between changes in surface plasmon resonance (SPR) spectra and degrees of surface coverage (Θ). In sections 2 and 3, UV−visible spectroscopy and time-dependent cryo-TEM imaging are used to investigate the kinetics and thermodynamics of monolayer self-assembly. The roles of POM charge, structure and counter cations are addressed in the Discussion section.

1. Preparation and Characterization of Anion-Ligand Monolayers on a Gold Nanoparticle. 1.1. Synthesis and Direct Imaging of Anion-Ligand Monolayers. Citrate-protected gold nanoparticles were reacted with a solution of α-$K_9AlW_{11}O_{39}$ (K_9**1**) (see Experimental section). The **1**-protected gold nanoparticles were characterized by TEM after drying on carbon-coated Cu grids. As is often the case for dried samples of POM-protected metal(0) nanoparticles,[5] the gold particles are embedded within an amorphous film of the POM salt (Figure S5, Supporting Information).

After using rapid cryogenic cooling to "trap" the solution-state structures of the **1**-protected gold nanoparticles in a "water-glass" matrix,[5] however, TEM images revealed a "ring" of individual molecules of **1** around the periphery of the metal particle (Figure 2). Panel A shows the citrate-stabilized gold

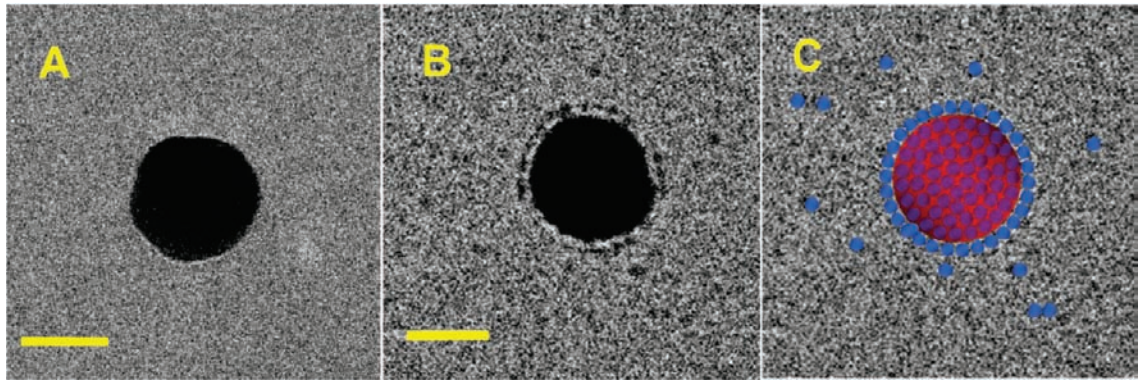

Figure 2. Cryo-TEM images of (A) citrate-protected and (B) **1**-protected gold nanoparticles. Panel **C** is a copy of the image in **B**, enhanced (solid blue circles) to highlight: (1) the "ring" of individual **1** anions at the periphery of the gold particle, (2) coverage of the particle's surface indicated by the presence of the peripheral ring, and (3) "freely solvated" molecules of **1** "trapped" in the vicinity of the gold particle in the water-glass matrix. Additional cryo-TEM images are included as Supporting Information (Figures S6 and S7). Scale bar = 10 nm.

particle before addition of **1**. Individual citrate molecules are not observed, such that the periphery of the particle appears smooth. By contrast, the heavy ($Z = 74$) nuclei of the 11 W atoms in each POM cluster scatter electrons much more effectively than do organic ligands. This makes it possible to resolve individual cluster-anion ligands[4a,d,e] as shown in panel B, the first reported image of protecting ligands on a gold nanoparticle in its native solution state. The image in panel B represents a 2-dimensional projection of the particle and its POM-protecting monolayer (individual molecules of **1** are highlighted in panel C). Scattering by the gold particle precludes observation of POM ligands on the superior and anterior surfaces the metal particle, while the spacing between molecules of **1** on the gold surface (discussed later in this section) makes it possible to image individual cluster anions.

Another feature of the image in panel B is the absence of ordered arrangements of **1** beyond the POM monolayer on the surface of the gold particle. In addition, the Debye length, κ^{-1}, of the particle in panel B is 1.0 nm (see the Supporting Information for details). This distance—from the Stern layer to the slipping plane—is slightly larger than the combined diameters of two hydrated K^+ counter cations (4.6 Å for each cation),[11b] which make up 95% of the counter cations present. The remaining 5% of the counter cations are Na^+.

1.2. Quantitative Analysis of the POM-Ligand Monolayer. To precisely correlate changes in the SPR with the formation of POM monolayers on the gold nanoparticles, the numbers of molecules of **1** in the peripheral rings of a number of well resolved 13.8-nm diameter gold nanoparticles were counted. For example, the 13.8 nm particle in Figure 2B displays a ring of 30 ± 1 molecules of **1** (see highlighted image in Figure S9, Supporting Information). For hexagonal packing, geometrical extrapolation from the perimeter ($2\pi r$) to the entire surface ($4\pi r^2$) gives a total of 330 ± 33 anions in the monolayer shell (see Supporting Information for details). Based on the surface area of the 13.8-nm diameter gold core, this corresponds to a ligand density of $7.4 \pm 0.7 \times 10^{-11}$ mol cm^{-2}.[24] For square packing, the 30 ± 1 molecules of **1** in the perimeter lead to 286 ± 29 ligands on the particle's surface, and a density of $6.4 \pm 0.6 \times 10^{-11}$ mol cm^{-2}. Hexagonal versus square packing cannot be discerned from cryo-TEM images. However, the numbers of ligands on each particle and respective surface densities calculated using the two packing models are very close to one another (i.e., within estimated uncertainties).

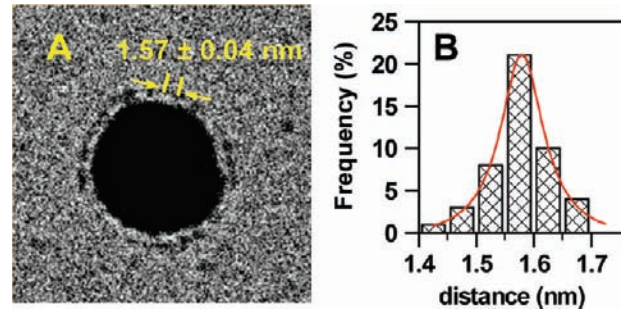

Figure 3. Geometrical analysis of gold-surface coverage by **1**. (A) Cryo-TEM image of a gold nanoparticle covered with a monolayer of **1**; the two arrows indicate the center-to-center distance between two adjacent molecules of **1**. (B) Range of values obtained for this measurement over a statistically meaningful number of particles and **1** anions.

Tentative support for hexagonal packing might be derived from scanning tunneling microscopy (STM) studies of Keggin anions on planar surfaces. Those data reveal square packing arrangements for short distances of ca. 1.0 to 1.1 nm between POM anions,[2c,d,f,26] and hexagonal packing for center-to-center distances greater than 1.3 nm.[2f,26] In this regard, measurement of over 100 center-to-center distances (Figure 3) gave a value of 1.57 ± 0.04 nm. Also, by assuming hexagonal packing, this distance gives a surface-coverage density of $7.8 \pm 0.4 \times 10^{-11}$ mol cm^{-2}, statistically identical to the value obtained (immediately above) from 330 molecules of **1** on each 13.8-nm particle. Finally, analysis of the distance from the gold surface to the centers of bound POM anions (Figure S10, Supporting Information) gives a value of 0.96 ± 0.04 nm. Due to the use of phase contrast, however, the actual distance may be shorter than this value.

(24) This is smaller than the value of $1.7-1.8 \times 10^{-10}$ mol cm^{-2} reported for $AsMo_{11}VO_{40}^{4-}$ on a planar Au(111) surface (ref 2d), while larger than the value of $4.3-4.9 \times 10^{-11}$ mol cm^{-2} for $SiW_{12}O_{40}^{4-}$ on a gold electrode (ref 25) (both values were obtained by quartz-crystal microbalance measurements). For adsorption of the Wells-Dawson anion, α_2-$P_2W_{17}O_{61}Cr^{III}(OH)_2^{7-}$, on a Hg(0) hanging-drop electrode, electrochemical analysis (ref 2h gave a coverage density of $\sim 7 \times 10^{-11}$ mol cm^{-2}, nearly identical to that found in the present work).

(25) Keita, B.; Nadjo, L.; Belanger, D.; Wilde, C. P.; Hilaire, M. *J. Electroanal. Chem.* **1995**, *384*, 155–169.

(26) (a) Song, I. K.; Shnitser, R. B.; Cowan, J. J.; Hill, C. L.; Barteau, M. A. *Inorg. Chem.* **2002**, *41*, 1292–1298. (b) Song, I. K.; Kaba, M. S.; Barteau, M. A. *J. Phys. Chem.* **1996**, *100*, 17528–17534.

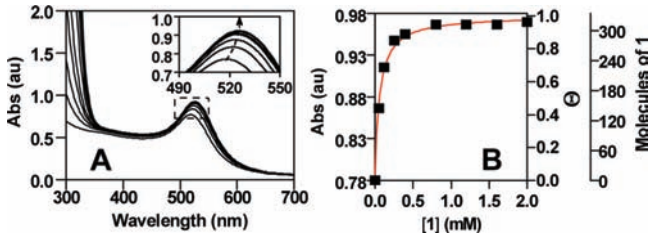

Figure 4. UV−visible absorbance spectra of citrate-protected gold nanoparticles (3.1×10^{-9} M) after incremental additions of α-$K_9AlW_{11}O_{39}$ (K_9**1**) in water. (A) Effect of [K_9**1**]: from bottom to top = 0.0, 0.05, 0.12, 0.25, 0.40, 0.80, 1.20, 1.60, and 2.00 mM, measured 20 h after mixing. The inset shows the gradual red shift in the absorbance maximum from 520 to 526 nm. (B) Change in the absorbance at 526 nm as a function of [K_9**1**]. Fractional coverage (Θ) of the gold surface by **1**, and the corresponding number of molecules of **1** on each gold particle, are indicated by the y-axes at the right of panel B. For square packing, the far-right *y*-axis would simply indicate 286 molecules for Θ = 1.

The diameters of the gold cores are 13.8 ± 0.9 nm. Thus, for 5.0×10^{-4} M solutions of Au (from $HAuCl_4$), the concentration of gold particles (density = 19.3 g/cm^3) is $6.2 \pm 1.3 \times 10^{-9}$ M. Assuming hexagonal packing, and 330 molecules of **1** bound to each gold particle, the concentration of occupied sites in the nanoparticle solution is $2.0 \pm 0.4 \times 10^{-6}$ M. This value now makes it possible to correlate the number of POM ligands on the gold nanoparticles with changes in the UV−vis spectral features[16b,c,22a−c,23] of the surface plasmon resonance.

2. Monolayer Formation. 2.1. Surface Coverage and the Surface Plasmon Resonance. The absorption maximum in UV−visible spectra of citrate-protected gold nanoparticles is located at 520 nm. Upon incremental additions of α-$K_9AlW_{11}O_{39}$ (K_9**1**), absorbance values increase until reaching a plateau, while the position of the absorbance maximum shifts from 520 to 526 nm (Figure 4). A corresponding color change is visible by eye (Figure S11, Supporting Information).

The functional dependence of absorbance on the concentration of **1** in panel B is characteristic of a type I Langmuir isotherm, for which, asymptotic approach to a finite value is indicative of monolayer formation. Using Mie theory (see Experimental section) and data from cryo-TEM images (Figure 2 and Figure S9, Supporting Information), the fractional coverage of the gold nanoparticle surface (Θ; *y*-axis at the right in panel B) was correlated with the number of POM ligands *on each gold particle* (right-most *y*-axis in panel B).

In further preparation for UV−visible spectroscopic study of POM-monolayer nucleation, growth and stability, two control experiments were performed. First, changes in the average protonation state of citrate upon additions of POM salts (indicated by small increases in pH values) had no appreciable effect on the SPR spectra (Figure S2, Supporting Information). Second, deliberate additions of large (>8 mM) concentrations of $Na_6H_2W_{12}O_{40}$ (Na_6**4**), a POM salt much more soluble than K_9**1**, showed that the changes observed in Figure 4 were not due to aggregation of the gold particles (Figure S12, Supporting Information).

2.2. Effects of POM Charge and Structure on Langmuir Isotherms. Langmuir isotherms[2d,27] were obtained for a series of POM anions. In order of incrementally decreasing anion charge, these were: the monodefect structures, α-$K_9AlW_{11}O_{39}$ (K_9**1**), α-$K_8SiW_{11}O_{39}$ (K_8**2**) and α-$K_7PW_{11}O_{39}$ (K_7**3**), and the plenary structures, α-$Na_6H_2W_{12}O_{40}$ (Na_6**4**) and α-$Na_5AlW_{12}O_{40}$ (Na_5**5**) (Figure 1).

The curves in Figure 5A (obtained at 526 nm) were fitted to eq 5, a Langmuir model derived in the Experimental section.

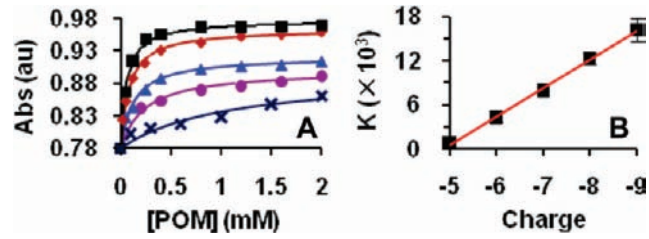

Figure 5. Adsorption isotherms for reactions of citrate-protected gold nanoparticles with a series of POM anions. (A) Absorbance versus POM concentration measurements for α-$K_9AlW_{11}O_{39}$ (K_9**1**; ■), α-$K_8SiW_{11}O_{39}$ (K_8**2**; ◆), α-$K_7PW_{11}O_{39}$ (K_7**3**; ▲), α-$Na_6H_2W_{12}O_{40}$ (Na_6**4**; ●) and α-$Na_5AlW_{12}O_{40}$ (Na_5**5**; ×). The curves are fits to eq 5. (B) Constants, *K* (from eq 5), plotted as a function of POM charge. In all cases, the concentration of gold nanoparticles was 3.1×10^{-9} M.

In eq 5, A_0 and A_1 correspond to "no surface-bound" POMs and to "complete surface coverage", respectively, [POM] is the total concentration of POM anions in solution, and *K* is a constant.

Data for adsorption of **1** (top curve in Figure 5A) gave an excellent fit to eq 5 ($R^2 > 0.995$).[28] Similarly good fits were obtained for anions **2** through **4**, and the fit for the 5- Keggin anion, **5** (bottom curve in panel A), was acceptable ($R^2 = 0.922$). Fitting of the data to eq 5 also provides values for A_1 (i.e., for Θ = 1; full surface coverage), from which it is possible to calculate the changes in absorbance associated with complete coverage, ΔA_{max} (= $A_1 - A_0$). As can be seen in Figure 5A, ΔA_{max} values increase with POM charge. For example, ΔA_{max} values increase from 0.147 to 0.189 to 0.207 absorbance units (a.u.) as POM charges increase from 7- to 8- to 9-, respectively, for **3**, **2** and **1**. Notably, this variation in ΔA_{max} is independent from calculated *K* values, which describe the *curvatures* of the plots in Figure 5A.

To confirm that *K* values from eq 5 indicate relative binding affinities, cryo-TEM images were obtained after reacting citrate-stabilized gold nanoparticles with 2.0 mM of **3** and 2.5 mM of **4**. According to data in Figure 5A and eq 4 (see Materials and Methods) this corresponds to ~94% and ~91% surface coverage by **3** and **4**, respectively. Cryo-TEM images (Figure S14, Supporting Information) are consistent with extensive but incomplete surface coverage by both. For 2 mM K_9**1**, by contrast, eq 4 gives 97% coverage, and more complete monolayer formation is consistently observed in cryo-TEM images (cf. Figure 2B). To establish the reversibility of POM adsorption, a citrate-protected gold-nanoparticle solution was made 0.04 mM in **1** (to give 40% coverage); after one day it was diluted to 0.02 mM **1** (i.e., to a theoretical coverage of 24% according to eq 4). No immediate change was observed. However, after warming the solution to 86 °C for 1.7 h (to overcome slow desorption),[29] and cooling to room temperature, the coverage had decreased to the theoretical value of 24%, as indicated by

(27) (a) Glomm, W. R.; Halskau, O.; Hanneseth, A. D.; Volden, S. *J. Phys. Chem. B* **2007**, *111*, 14329–14345. (b) Kaufman, E. D.; Belyea, J.; Johnson, M. C.; Nicholson, Z. M.; Ricks, J. L.; Shah, P. K.; Bayless, M.; Pettersson, T.; Feldoto, Z.; Blomberg, E.; Claesson, P.; Franzen, S. *Langmuir* **2007**, *23*, 6053–6062. (c) Brewer, S. H.; Glomm, W. R.; Johnson, M. C.; Knag, M. K.; Franzen, S. *Langmuir* **2005**, *21*, 9303–9307. (d) Kirk, J. S.; Bohn, P. W. *J. Am. Chem. Soc.* **2004**, *126*, 5920–5926. (e) Schessler, H. M.; Karpovich, D. S.; Blanchard, G. J. *J. Am. Chem. Soc.* **1996**, *118*, 9645–9651.

(28) The addition of citrate (1 to 2.5 mM) had no effect on the isotherms or associated *K* values for adsorption of **1** (Figure S13, Supporting Information), an indication that **1** is a significantly better ligand than citrate.

a *blue shift* of the SPR maximum and a *decrease* in its intensity (Figure S16, Supporting Information).

Constants, K, from eq 5 range from 930 M^{-1} for α-$Na_5AlW_{12}O_{40}$ (Na_5**5**) to 16,250 M^{-1} for α-$K_9AlW_{11}O_{39}$ (K_9**1**),[30] and are plotted as a function of POM-anion charge in Figure 5B (see Table S1 for a tabular listing with uncertainties, Supporting Information). Surprisingly, the K values increase linearly with POM charge, despite significant structural differences between the plenary alpha-Keggin anions, **4** and **5** (Na^+ salts), and the monodefect derivatives, **1**, **2** and **3** (K^+ salts).[31] This suggests that *charge* is more important than anion *structure* in determining extents of surface coverage. Gewirth[2b] by contrast, has shown that for the self-assembly of **2** on *planar* Ag(111) surfaces, specific POM orientations relative to Ag binding sites are involved. Three notable differences in the present work are: (1) the use of Au(0), which is less effective than Ag(0) at binding POM anions,[32] (2) the presence of surface curvature for the Au(0) nanoparticles, versus *planar* Ag(0), and (3) the presence of vertices, edges and terraces on surface of each Au(0) nanoparticle, versus uniform Ag(111). The present findings are consistent, however, with the beneficial effect of larger anion charges on the abilities of structurally different POMs to control the reduction of Ir(I) to Ir(0) nanoparticles in organic solvents.[9a]

2.3. Initial POM Association with the Gold-Nanoparticle Surface (Nucleation). Solutions of 13.8 nm gold nanoparticles and POMs were rapidly combined using a stopped-flow instrument, and initial rates for association of POM anions with the gold-particle surface were quantified by changes with time in the SPR maximum (520 nm for the citrate-protected particles). Rates of POM-gold association were determined as functions of gold-nanoparticle concentration ([Au NP]) at constant [**1**], and of [POM] (POM = **1**, **2**, **3**) at constant [Au NP]. Changes in ionic strength had notable effects on initial rates (rates increased with ionic strength; see Figure S3, Supporting Information), while control experiments showed that citrate behaved primarily as an electrolyte, that is, kinetic inhibition was not observed (Figure S4, Supporting Information). Therefore, citrate buffers were used to maintain constant ionic strength values.[33] Surface coverage values, calculated from changes in SPR absorbance over the first 10 s of reaction, were always <3.4%. For 330 POM anions per complete monolayer (hexagonal packing), this corresponds to <12 POMs per gold nanoparticle; for square packing, this gives <10 POM anions. Because the POM anions approach the gold particles from all directions, they are assumed to be independent from one another at first encounter with the gold surface (i.e., the "nucleation" phase of monolayer growth).

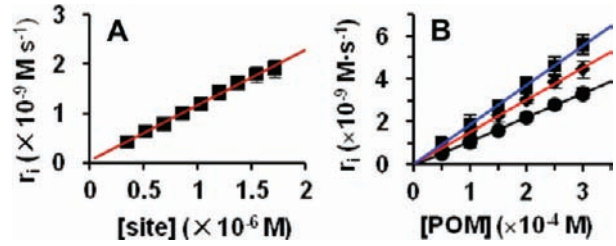

Figure 6. (A) Initial rates versus the molar concentration of binding (occupancy) sites ([site]) on gold nanoparticles at constant [**1**] (0.15 mM) and ionic strength (15.3 mM). (B) Initial rates versus concentrations of **1** (●), **2** (◆) and **3** (■), at a constant [site] of 1.0×10^{-6} M.

At constant [K_9**1**] (0.15 mM) and ionic strength (15.3 mM), initial rates varied linearly with the concentration of available sites on gold ([site] in Figure 6A; $R^2 = 1.00$), indicative of a first-order dependence. Concentrations of 3 POM salts, K_9**1**, K_8**2**, and K_7**3**, were then varied at constant [Au NP] (Figure 6B). For reactions of each POM salt, ionic strength values corresponded to the largest POM concentrations used ([POM] = 0.3 mM). As a result, ionic-strength values varied slightly from 17.6 to 14.9 to 12.2 mM for reactions of **1**, **2**, and **3** (9-, 8- and 7- anions, respectively).

The linear plots show that initial association of each of the 3 POM anions with the gold surface is first order in [POM]. The apparent rate constants, k_{app} for the association of **1** with gold in panel A (slope of the plot divided by [K_9**1**]) is 7.5 ± 0.2 M^{-1} s^{-1}. This is in reasonable agreement with the value of k_{app} = 11.6 ± 0.2 M^{-1} s^{-1} for [K_9**1**] (from panel B), obtained from a different sample of gold nanoparticles and at a different ionic strength. These data lead to the bimolecular rate expression in eq 7.

$$\text{Rate of initial association}(\text{"nucleation"}) = k_{app}[\text{site}][\text{POM}] \quad (7)$$

To quantify the effect of anion charge on initial rate values, data for all 3 POM anions (panel B) were obtained using the *same gold nanoparticle solution*. For the 3 POMs, k_{app} values decreased with anion charge in the order: 18.9 M^{-1} s^{-1} for **3** (7-) to 15.2 M^{-1} s^{-1} for **2** (8-) to 11.6 ± 0.2 M^{-1} s^{-1} for **1** (9-) (these values are plotted in Figure S17, Supporting Information). These rate constants are many orders of magnitude smaller than the diffusion-controlled limit (>10^9 sec^{-1}), which indicates the presence of a significant kinetic barrier to POM-gold association. The apparent sensitivity of rate constants to POM charge suggests that spontaneous desorption of citrate (i.e., a dissociative mechanism[34]) is not kinetically significant. However, direct displacement of citrate ligands from the gold surface by incoming POM anions could be rate limiting (an associative mechanism[15c,35]). Whether or not that is the case, the electric potential of the negatively charged citrate-protected gold

(29) For the reaction of K_9**1** with gold nanoparticles, the SPR absorption reaches a plateau within one day, after which surface coverage, Θ, remains constant for days to weeks, even though [POM] ≫ [site] (Figure S15, Supporting Information). While this is consistent with equilibrium control, desorption of POMs from mixed- (citrate + POM) ligand shells is slow at room temperature, which suggests that the energetic barriers to desorption are considerable; see Results section 3.1.

(30) These values are consistent with those obtained by Dong and co-workers (ref 2d) where K = 3700 M^{-1} for $AsMo_{11}VO_{40}^{4-}$ on a Au(111) surface.

(31) On the basis of a set of experimental criteria, more negatively charged POM anions appear to better stabilize Ir(0) nanoparticles in organic solvents (this is one implication of the data in ref 9a). However, the linear relationship in Figure 5B is unprecedented. A detailed investigation of this linear correlation is in progress.

(32) Teague, C. M.; Li, X.; Biggin, M. E.; Lee, L.; Kim, J.; Gewirth, A. A. *J. Phys. Chem. B* **2004**, *108*, 1974–1985.

(33) Citrate could be added without causing aggregation of the gold particles. Ionic-strengths were calculated using published pK_a values for citric acid and experimental pH values to estimate the concentrations of species present (citric acid and its mono- and di-basic forms). The product of the 2e^--oxidation of citrate by Au(III) during nanoparticle synthesis was assumed to be present as the mono-anion (e.g., $HO_2CCH_2C(O)CH_2CO_2^-$) at pH 6.

(34) (a) Ionita, P.; Caragheorgheopol, A.; Gilbert, B. C.; Chechik, V. *Langmuir* **2004**, *20*, 11536–11544. (b) Ionita, P.; Caragheorgheopol, A.; Gilbert, B. C.; Chechik, V. *J. Am. Chem. Soc.* **2002**, *124*, 9048–9049.

(35) (a) Kassam, A.; Bremner, G.; Clark, B.; Ulibarri, G.; Lennox, R. B. *J. Am. Chem. Soc.* **2006**, *128*, 3476–3477. (b) Templeton, A. C.; Wuelfing, W. P.; Murray, R. W. *Acc. Chem. Res.* **2000**, *33*, 27–36.

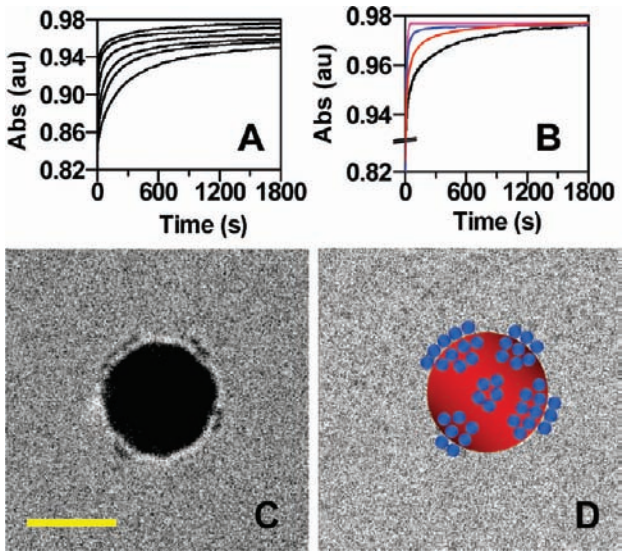

Figure 7. UV−visible spectroscopic and cryo-TEM study of monolayer growth and formation. (A) Increase in absorbance of the SPR as a function of time after adding incrementally larger concentrations of K_9**1** (from 0.4 to 2.0 mM at $t = 0$ s) to a fixed concentration of gold nanoparticles (3.1×10^{-9} M) (values refer to concentrations after mixing). (B) Comparison of data for a representative curve in panel A (2 mM **1**) with three kinetic models[35a,39] for monolayer formation: pseudofirst order (pink curve), pseudosecond order (blue curve) and a Langmuir diffusion-limited model (red curve). (C) Time-dependent cryo-TEM image of a citrate-protected gold nanoparticle after 40% surface coverage by **1** ($\Theta = 0.4$). (D) Illustration showing how the image in panel C implies the presence of "islands" (discrete regions) of POMs on the gold surface. The "empty" areas in the illustration are protected by citrate anions. Bar = 10 nm.

particles presents a significant kinetic barrier to approach of the POM anions. The zeta potential, ζ, of the citrate-protected gold particles is −31.5 mV, which gives an effective negative charge at the "slipping plane" (within the diffuse component of the electric double layer) of 15.0*e*.[36] This presents a kinetic barrier proportional to $\exp(-q\zeta/RT)$ where q is the charge of the approaching anion and ζ is the zeta potential of the particle.[38] This energetic barrier not only contributes to the relatively small k_{app} values reported here, but may also explain why k_{app} values *decrease* as POM-anion charges increase from 7- to 8- to 9-.

2.4. Kinetics and Structural Evolution of the POM Monolayer. The rate of monolayer growth and "completion" was evaluated by measuring the change with time of the SPR maximum (526 nm) after addition of K_9**1** to the citrate-protected 13.8 nm gold nanoparticles. Data for the rapid initial increase in absorbance were obtained using a stopped-flow mixing apparatus, and the reaction was monitored for a total of 30 min (1800 s; Figures 7A).

Monolayer formation involves a smooth progression from a relatively rapid early growth phase to a much slower phase for approach to full coverage ($\Theta = 1$). (Similar results were obtained for reactions of **2** and **3**; see Figure S18, Supporting Information.) The half-lives ($t_{1/2}$) for monolayer formation (times needed to reach $\Theta = 0.5$), obey a well-behaved—yet empirical—exponential function of [**1**] (Figure S19, Supporting Information). When data obtained using **1** are fitted to classical kinetic models[35a,39] for the formation of monolayers of neutral ligands such as thiols on metal surfaces, however, the change from rapid to slow phases is slightly slower than predicted by the models (Figure 7B). To investigate this in more detail, time-dependent cryo-TEM imaging was used to observe a growing POM monolayer during an intermediate stage of its self-assembly.

Prior to cryo-TEM imaging, UV−visible spectroscopy was used to determine the time needed after addition of **1** to reach 40% POM coverage ($\Theta = 0.4$). Solutions of K_9**1** and of the gold nanoparticles were combined at $t = 0$, and at the determined time after mixing, the evolving solution-state structure was cryogenically cooled. A representative cryo-TEM image is provided in Figure 7C, and additional images are provided as Supporting Information (Figure S20). The images reveal discrete groupings of **1** at the perimeter of the gold particle, which indicate the presence of "islands" or "patches"[40] of POM anions. This is highlighted in Figure 7D, an illustration of a surface structure implied by the image in panel C.

This "island" growth mechanism is analogous to that observed by Gewirth for the formation of ordered silicotungstate monolayers on planar Ag(111),[2g] and by Poirier for the formation of alkanethiol monolayers on planar Au(111).[17] To our knowledge the image in Figure 7C is the first direct support for this growth mechanism on a metal nanoparticle. The observation of "islands" points to strong interactions between the POM anions: once a polyanion is adsorbed, adjacent sites become more favored for binding of the next POM anion. This is most likely due to electrostatic forces between POMs and their counter cations, and/or to hydrogen bonds between POMs and cation-bound water molecules,[41] and is consistent with a structural role for counter cations within the POM-monolayer shell (see Discussion section).

3. Monolayer Stability and the Gold/Ligand Interface.

3.1. Ligand Desorption. UV−visible spectroscopy was used to investigate desorption of **1** from "islands" and fully formed monolayers. For this, concentrations of **1** sufficient to give incrementally greater degrees of surface coverage were added to citrate-protected gold nanoparticles. In all cases, these solutions contained large excesses of **1**. After final absorbance values were reached (~1 day), the solutions were rapidly diluted by stopped-flow mixing with equal volumes of pure water (i.e., 50% dilution within ca. 30 msec).[15a] No changes were observed at 526 nm for at least 200 s (Figures 8A) and for up to 1 day (not shown). This implies that the "islands", as well as fully formed monolayers, possess substantial kinetic stabilities. Hence, the energetically favorable interactions that give rise to "island"-like organizations of POM anions during monolayer growth impart substantial kinetic stabilities to these discrete nanoscale domains.

Cryo-TEM imaging was used to confirm the kinetic stabilities implied by the data in Figure 8A. For this, **1**-monolayer

(36) The charge, q, is related to the zeta potential, ζ, by $q = 4\pi\epsilon r\zeta$ (ref 37), where $\epsilon = 80 \times 8.9 \times 10^{-12}$ F m^{-1} in water at 298K, and r is the radius of the particle. For the citrate-protected gold nanoparticles, $r \approx 8.5 \times 10^{-9}$ m (including an estimated ~1.6 nm thick citrate layer), $\zeta = -31.5 \times 10^{-3}$ V, and $q = 2.4 \times 10^{-18}$ C. Taking the charge of an electron as 1.6×10^{-19} C, one obtains q = 15.0*e*.

(37) Chen, I. *Langmuir* **1996**, *12*, 3437–3441.

(38) MacRitchie, F. *Chemistry at Interfaces*; Academic Press, Inc.: New York, 1990.

(39) (a) Tamerler, C.; Oren, E. E.; Duman, M.; Venkatasubramanian, E.; Sarikaya, M. *Langmuir* **2006**, *22*, 7712–7718. (b) Georgiadis, R.; Peterlinz, K. P.; Peterson, A. W. *J. Am. Chem. Soc.* **2000**, *122*, 3166–3173.

(40) Zhang; Glotzer, S. C. *Nano Lett.* **2004**, *4*, 1407–1413.

(41) (a) Yuan, L.; Qin, C.; Wang, X.; Li, Y.; Wang, E. *Dalton Trans.* **2009**, 4169–4175. (b) Wang, J.; Feng, Y.; Ma, P.; Niu, J. *J. Coord. Chem.* **2009**, *62*, 1895–1901. (c) Zhou, Y.; Yin, J.; Zhang, L. *J. Mol. Struct.* **2009**, *920*, 61–67. (d) Lee, K. Y.; Arai, T.; Nakata, S.; Asaoka, S.; Okuhara, T.; Misono, M. *J. Am. Chem. Soc.* **1992**, *114*, 2836–2842.

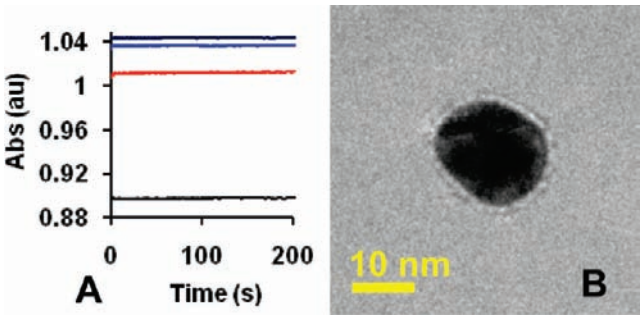

Figure 8. Kinetic stabilities of discrete domains and complete monolayers of **1** on 13.8 nm gold nanoparticles. (A) Dilution kinetics (after rapid mixing) of solutions containing 0.0, 0.05, 0.13, and 1.5 mM K_9**1** and (B) a cryo-TEM image of a monolayer of **1** after removal of excess (2 mM) **1** from bulk solution by centrifugation and redispersion, which reduced the bulk concentration of **1** to 3×10^{-6} M.

protected gold nanoparticles were separated from excess K_9**1** (initially 2 mM) and citrate by centrifugation (5 min at 14000 rpm), followed by redispersion in pure water (some aggregation was noted by UV−visible spectroscopy). Excess NaCl was added to a small sample of this solution to precipitate the gold particles, and the concentration of residual **1** in the resultant colorless solution was quantified by UV−vis spectroscopy at 262 nm; see Figure S21, Supporting Information. The residual [**1**] was ca. 3.1×10^{-6} M, close to the total concentration of "occupancy" sites on the gold nanoparticles, 1.0×10^{-6} M. The redispersed solution is quite stable: no precipitate or spectroscopic changes were observed after one month at room temperature. Cryo-TEM images obtained 3 days after centrifugation and redispersion revealed the presence of intact monolayers of **1** on the gold surface (Figure 8B). Now, however, few or no POM anions are observed in the vicinity of the particle (e.g., compare with Figures 2B and C). The image in Figure 8B directly confirms the presence of significant kinetic barriers to desorption of **1**. This is consistent with similar observations for POM anions on planar Ag(111)[2g] and Au(111)[2d] surfaces. In both these cases, POM regions and monolayers remained intact after immersion in pure water.

3.2. Gold/Ligand Interface. The redispersed solution was then dried on a carbon-coated Cu grid and analyzed by traditional TEM and HRTEM. No aggregation was observed. Due to the drying, however, individual molecules of **1** seen in Figure 8B were no longer discernible. Rather, the POMs were observed as an amorphous ca. 1.5 nm thick shell.[42] Fourier transform analyses of the HRTEM images showed some particles to be single crystals (Figure S22, Supporting Information). Other particles were polycrystalline, and many exhibited stacking errors and twinning. These random and in many cases kinetically controlled defects, in combination with the pseudospherical shape of the gold particles, are consistent with a high surface density of edges and vertices at the intersections of numerous small facets of the highly truncated gold core.

This is pertinent to understanding structure and bonding at the ligand/metal(0) interface, an important issue in the rational design of functional POM- and other ligand-modified metal(0)-nanoparticles.[9d,10,16a,b] Finke has proposed that "lattice matching" between terminal or bridging oxide ligands of POMs and specific lattice planes render some POM ligands better at stabilizing metal(0) nanoparticles,[9b] but more recently has shown that ligand *charge* also plays an important role.[9a] The present work supports the latter view. Particles observed by cryo-TEM consistently possess effectively complete peripheral rings of POMs, even though these monolayers must span all the lattice-plane edges and vertices around the pseudospherical (single-crystal or polycrystalline) gold cores. This suggests that close lattice matching is not energetically and structurally imperative. For *planar* metal surfaces, lattice matching clearly determines the orientations of POM structures to the metal surfaces.[2b,c,f,g] For nanoparticles, however, the available data suggest that lattice matching and charge are *both* involved, with the relative importance of each probably determined by the size and surface-atom structure of the metal(0) particle, the charge and structure of the POM, solvent, and the nature of the POM counter cations.

Discussion

The cryo-TEM images reported here reveal organizations of α-$AlW_{11}O_{39}^{9-}$ (**1**) on a 13.8-nm diameter gold core. Building on this structural information, kinetic and thermodynamic data were used to investigate monolayer nucleation, growth and stability. These data also made it possible to define the conditions needed to observe POM-monolayer growth in "real time" by time-dependent cryo-TEM. Those images—the first of their kind for a metal nanoparticle—reveal that monolayer growth occurs via the organization of individual molecules of **1** into kinetically stable "islands" on the gold surface. The formation of these nanodomains points to a net attraction between the highly negatively charged (9-) anions. We now show how analysis of ligand and particle charge, and of the observed distances between bound POM anions, leads to the conclusion that counter cations must be structurally integrated into the inorganic ligand shell. This model is then used to better understand observed effects of ligand charge and structure on monolayer formation and stability.

Counter Cations and the Energetics of Monolayer Formation. Based on cryo-TEM images and hexagonal packing, each particle contains 330 molecules of **1**. Therefore, in the absence of counter cations, each **1**-protected particle would possess an unreasonably large charge of 2970-. The displacement of citrate and self-assembly of the POM monolayer results in a shift in zeta potential from −31.5 mV to −62.1 mV. These experimental values assign charges of 15.0*e* and 29.5e (i.e, effectively 15- and 29.5-) to the citrate- and **1**-protected[43] gold nanoparticles. For the **1**-protected particles, this means that 99%—2940 out of 2970—of the POM counter cations lie within the "slipping plane", that is, one Debye length, κ^{-1}, outside the Stern layer (Figure S8, Supporting Information). As noted above (see Results section), $\kappa^{-1} = 1.0$ nm, while the thickness of the Stern layer is less than or equal to the diameter of a single hydrated K^+ countercation (4.6 Å). Hence, the Stern-layer thickness and Debye length sum to ≤ ∼1.5 nm. Therefore, 99% of the K^+ counter cations are located ≤1.5 nm from the outer surface of the POM shell.

Furthermore, structurally based energetic arguments indicate that numerous K^+ ion are structurally integrated into the monolayer shell itself.[3d,44] Cryo-TEM images (Figure 3) indicate that the average distance between the centers of neighboring

(42) Zhang, G.; Keita, B.; Dolbecq, A.; Mialane, P.; Sécheresse, F.; Miserque, F.; Nadjo, L. *Chem. Mater.* **2007**, *19*, 5821–5823.

(43) For **1**-protected Au NPs, $r = 8.5 \times 10^{-9}$ m and $\zeta = -62.1 \times 10^{-3}$ V, so that $q = -4.7 \times 10^{-18}$ C, or −29.5 e (see ref 36).

(44) (a) Laaksonen, T.; Ahonen, P.; Johans, C.; Kontturi, K. *ChemPhysChem* **2006**, *7*, 2143–2149. (b) Schweiss, R.; Pleul, D.; Simon, F.; Janke, A.; Welzel, P. B.; Voit, B.; Knoll, W.; Werner, C. *J. Phys. Chem. B* **2004**, *108*, 2910–2917.

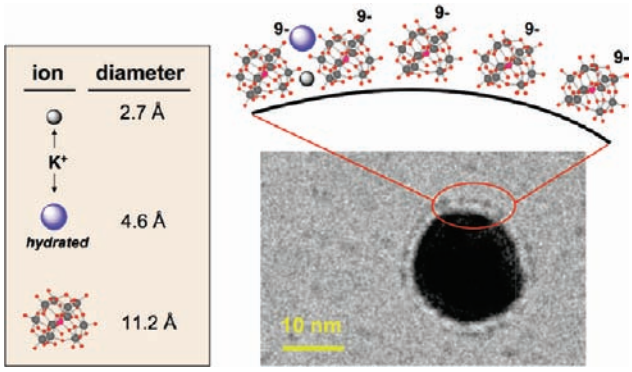

Figure 9. Scale model of α-$AlW_{11}O_{39}^{9-}$ (**1**) and K^+ counter cations on the surface of a gold nanoparticle. The key at left shows the crystallographic and hydrated sizes of K^+ relative to a scale model of **1**. The structures of **1** on the gold surface are drawn with their defect sites facing the gold surface,[2b,9b,10h] although this may not be the only viable orientation.

POM anions is 1.57 ± 0.04 nm. Based on hexagonal packing, each molecule of **1** lies at an equal distance from 6 nearest neighbors. The electrostatic "work" needed to place a molecule of **1** at the observed distance from each of these 6 nearest neighbors is estimated to be 80 kcal mol^{-1}. This value was obtained by calculating the Coulombic "work" needed to bring the seventh anion into the center of the hexagonal arrangement at 15 mM ionic strength and 298K.[14a] Anion repulsions between the 6 anions already present were not included. The 80 kcal mol^{-1} of "work" from repulsion by the nearest-neighbor anions gives an association constant (from $\Delta G° = -RT\ln K$) of $K \approx 10^{-60}$. For square packing (4 nearest neighbors), these values remain large: 53 kcal mol^{-1} of "work" and an association constant of $K \approx 10^{-40}$. For comparison, adsorption Gibbs free energies for bonds between alkanethiols and gold surfaces are favorable by up to 20 kcal mol^{-1}.[27e,45] *Clearly, many counter cations are structurally integrated into the POM shell;*[3d] *without them, monolayer formation would be energetically prohibitive.*

Structural Role for Counter Cations in the Anion-Ligand Shell. Figure 9 shows five molecules of **1** at actual center-to-center distances (drawn to scale) on the gold nanoparticle surface, and spheres that represent the relative crystallographic (gray) and hydrated (blue) sizes of K^+ (see legend at the left of the figure).[46] Subtraction of the diameter of the Keggin anion (1.12 nm) from the center-to-center distance of 1.57 nm leaves 4.5 Å *between* molecules of **1** on the gold surface. Notably, the fully solvated K^+ cation, with its ~17 waters of hydration,[11b] drawn to scale near the outer region of the monolayer, is effectively the same size as the space between molecules of **1**. A fully dehydrated cation is shown closer to the metal surface. There, the hydrophobic character of the gold surface might facilitate partial dehydration of K^+, a process that would be compensated for by direct bonds between K^+ and the bridging and terminal O^{2-} ligands of the POM. In both cases (hydrated or partially dehydrated), aqua ligands on K^+ could form H-bonds to O^{2-} ligands of **1**.[47]

This electrostatic model is based on the documented roles of cations and H-bonding in numerous single-crystal X-ray diffraction studies of POM salts,[41] and is consistent with an early proposal by Anson[2h] for high-density surface coverage of hanging-drop Hg electrodes by POM salts in water. More generally, these findings are consistent with small distances between Keggin anions on planar surfaces when only small H^+ counter cations are present (i.e., a center-to-enter distance of 1.02 nm for molecules of α-$SiW_{12}O_{40}^{4-}$ on Ag(100) in acid solution),[2c] larger, cation-size dependent distances between POMs on planar graphite,[2f] and recent SAXS data that demonstrate the presence of structural counter-cations[48] in *hollow* single-walled POM-macroanion vesicles.[49] In light of the structural role of counter cations in the walls of macroanion vesicles, the gold cores in the present work appear to serve as templates for the formation of cation-stabilized monolayer shells. This aspect of POM-protected metal-nanoparticle structure has not been emphasized in previous studies, probably because, until recently,[5] there was no definitive evidence that POMs form well-ordered monolayers on metal(0) surfaces, and no detailed information about the structure of the POM ligand shell.

Electrostatic Stabilization and POM Orientation. Additional herein-reported findings are consistent with monolayer stabilization by structural integration of counter cations, and that this can be more important than orientation to the gold surface (i.e., "lattice matching"):[9b] (1) Time-dependent cryo-TEM imaging reveals that monolayer growth occurs via the formation of "islands" (Figure 7C), and dilution studies show that these discrete inorganic nanodomains possess significant kinetic stabilities (Figure 8A). (2) Completed monolayers possess considerable kinetic stabilities (Figure 8A), and cryo-TEM images demonstrate that they remain intact after redispersion in pure water (Figure 8B). (3) Type I Langmuir isotherms for a series of five plenary and monodefect Keggin anions reveal a linear (i.e., *structurally independent*) correlation between anion charge and affinity to the gold surface (Figure 5B). This is consistent with more energetically favorable ion-pair interactions within the monolayer shells of the more highly charged anions. "Lattice matching", based on specific POM structure and orientation, appears to be less important. (4) Consistent with this, the POM monolayer spans edges and vertices at numerous intersections of lattice-plane terraces on the surface of the pseudospherical gold nanoparticle (Results section 3.2).

Conclusions

Cryogenic "trapping" of aqueous solution-state structures was used to obtain the first TEM images of self-assembled monolayers of inorganic anions on a gold nanoparticle. This unique structural information made it possible to study the formation of a protecting-anion monolayer on a gold nanoparticle in unprecedented detail. Mie theory and UV−visible spectroscopy, combined with a *structurally based* interpretation of changes

(45) (a) Kirk, J. S.; Bohn, P. W. *J. Am. Chem. Soc.* **2004**, *126*, 5920–5926. (b) Karpovich, D. S.; Blanchard, G. J. *Langmuir* **1994**, *10*, 3315–3322.

(46) To form monolayers of **1**, the K^+ salt of the POM (2 mM **1** and 18 mM K^+) is in solution with 1 mM Na^+ (from trisodium citrate used in synthesis). As such, the molar ratio of K^+ to Na^+ is 18:1 (i.e., 95% K^+).

(47) More generally, favorable electrostatic interactions stabilize counter cations between bound POM anions just as hydrophobic interactions draw organic molecules into the organic shells of alkanethiol-protected gold nanoparticles, see: Lucarini, M.; Franchi, P.; Pedulli, G. F.; Pengo, P.; Scrimin, P.; Pasquato, L. *J. Am. Chem. Soc.* **2004**, *126*, 9326–9329.

(48) Antonio, M. R.; Nyman, M.; Anderson, T. M. *Angew. Chem., Int. Ed.* **2009**, *48*, 6136–6140.

(49) (a) Pigga, J. M.; Kistler, M. L.; Shew, C.; Antonio, M. R.; Liu, T. *Angew. Chem., Int. Ed.* **2009**, *48*, 6538–6542. (b) Zhang, J.; Keita, B.; Nadjo, L.; Mbomekalle, I. M.; Liu, T. *Langmuir* **2008**, *24*, 5277–5283. (c) Kistler, M. L.; Bhatt, A.; Liu, G.; Casa, D.; Liu, T. *J. Am. Chem. Soc.* **2007**, *129*, 6453–6460. (d) Liu, T.; Diemann, E.; Li, H.; Dress, A. W. M.; Müller, A. *Nature* **2003**, *426*, 59–62. (e) Liu, T. *J. Am. Chem. Soc.* **2003**, *125*, 312–313.

in the surface plasmon resonance (SPR), were then used to investigate the kinetics and thermodynamics of monolayer formation.

These data, in combination with zeta-potential measurements, time-dependent cryo-TEM images and energetic considerations, reveal an important structural role for alkali-metal counter cations in the POM ligand shell. This conclusion is consistent with an analogous role for counter cations in highly organized arrays of POM anions on planar surfaces[2,25,26] and within the single-walls of hollow POM-macroanion vesicles.[49] Hence, similar electrostatic considerations play an important role whether POM anions are found in monolayer arrays on planar surfaces, serve as protecting-ligands on metal nanoparticles,[5,10] or are present as components of hollow vesicles. As such, the data provided here not only provide new information for the rational design of functional POM-protected metal(0) nanoparticles, but more generally, establish a unifying principle for better understanding the self-assembly of supramolecular structures from metal-oxide cluster anions and other charged molecular building blocks.

Acknowledgment. I.A.W. thanks the Toman Foundation (Ben Gurion Univ.) and the ISF (248/09, 1667/09 and 1720/08) for support, E. Nativ-Roth for cryo-TEM images, L. Zeiri for Raman spectra, and Prof. A. A. Gewirth for valuable comments. Y.W. thanks the Israeli Ministry of Education for a Post-Doctoral Fellowship.

Supporting Information Available: TEM, HRTEM and cryo-TEM images, control experiments for kinetic and thermodynamic investigations, derivations, calculations and discussion. This material is available free of charge via the Internet at http://pubs.acs.org.

JA907815D